Plasmon-loss imaging of polymer-methanofullerene bulk heterojunction solar cells

Budhika G. Mendis, Sarah J. Bishop, Chris Groves, Marek Szablewski, Adam Berlie, and Douglas P. Halliday

Citation: Applied Physics Letters **102**, 253301 (2013); doi: 10.1063/1.4812485
View online: http://dx.doi.org/10.1063/1.4812485
View Table of Contents: http://scitation.aip.org/content/aip/journal/apl/102/25?ver=pdfcov
Published by the AIP Publishing

Plasmon-loss imaging of polymer-methanofullerene bulk heterojunction solar cells

Budhika G. Mendis,[1] Sarah J. Bishop,[1] Chris Groves,[2] Marek Szablewski,[1] Adam Berlie,[1] and Douglas P. Halliday[1]
[1]*Department of Physics, Durham University, South Road, Durham DH1 3LE, United Kingdom*
[2]*Department of Engineering and Computer Science, Durham University, South Road, Durham DH1 3LE, United Kingdom*

(Received 12 April 2013; accepted 12 June 2013; published online 25 June 2013)

The plasmon feature in an electron energy loss spectrum provides unique insight into poly(3-hexylthiophene) (P3HT)-phenyl-C61-butyric acid methyl ester (PCBM) solar cells. Analysis of the intensity, shape, and energy of the plasmon reveals information about the type of phase, distribution of P3HT semi-crystalline fibres, and PCBM packing density at high spatial resolution. Plasmon-loss imaging has also revealed nano-scale residual solvent pockets with preferentially dissolved PCBM. A robust tomography method for reconstructing the 3D morphology of the bulk heterojunction thin-film via plasmon-loss images is also presented. The analysis techniques can be used to investigate morphology evolution during thin-film processing and its effect on device performance.
 [http://dx.doi.org/10.1063/1.4812485]

The donor and acceptor phase separated morphology in an organic bulk heterojunction (BHJ) solar cell is crucial to producing efficient devices.[1] For example free carriers are generated by fully dissociating photogenerated excitons at the donor-acceptor interface. Since the exciton diffusion distance is only ∼10 nm in polymers, this process ideally requires a small domain size. Following exciton dissociation the free carriers must have contiguous percolation pathways to drift/diffuse towards the collection electrodes, a process which is favoured by larger sized domains. Processing methods such as thermal,[2] solvent,[3] annealing, and solvent additives[4] improve device efficiency by modifying the active layer morphology. Transmission electron microscopy (TEM) is an ideal technique for probing morphology at nanometre length scales, but in the case of BHJ solar cells imaging is complicated by the low contrast between the carbon-rich donor and acceptor phases. Nevertheless the 3D morphology of BHJ solar cells has been characterized using bright field electron tomography[5,6] where the contrast was enhanced by defocussing the objective lens. The defocussing degrades the spatial resolution, so that finer scale features may not be observed. Other artefacts of coherent imaging, such as Fresnel fringing, non-uniform amplitude contrast for the different spatial frequencies, and contrast reversals for features smaller than the point resolution, may also complicate tomographic reconstruction.

Herzing *et al.*[7] have shown that for poly(3-hexylthiophene) (P3HT)-phenyl-C61-butyric acid methyl ester (PCBM) bulk heterojunction solar cells the contrast can be improved by imaging with electrons that have lost energy to the material via plasmon excitations. The plasmon-loss images at different specimen tilts were used to reconstruct the 3D volume as in a conventional tomography experiment. A disadvantage of this method, as noted by the authors, is that the plasmon signal is not proportional to the projected specimen thickness and therefore does not satisfy the projection criterion for tomography (for small thicknesses however the relationship is linear to first order). This limits its value for BHJ solar cells which need to be sufficiently thick (∼100 nm) for efficient light absorption. Furthermore in electron tomography the projected specimen thickness is increased by a factor of ×3 at the high specimen tilts of ∼70°. In this paper a method to correct for non-linear thickness effects in plasmon-loss tomography is presented. It is also shown that the plasmon signal reveals a wealth of information about the BHJ morphology, such as the nature of the phase (P3HT or PCBM), PCBM packing density, and the presence of open channels, possibly due to solvent trapped within the active layer.

The sample investigated is a P3HT-PCBM solar cell containing 12 ± 5 nm diameter nanoparticles of Cu_2ZnSnS_4 (CZTS) prepared by the methodology of Guo *et al.*;[8] the nanoparticles are ideal as internal markers for aligning images in the tomography tilt series. The active layer was spin coated from equal volumes of chlorobenzene solution containing P3HT, PCBM (each 10 mg/ml), and toluene containing the CZTS nanoparticles (6 mg/ml). Spin coating was done at 1000 rpm for 1 min onto an ITO coated glass substrate with PEDOT:PSS (poly(3,4-ethylenedioxythiophene)-poly(styrenesulfonate)) layer, which is water soluble, thereby enabling the film to be released by immersing in de-ionized water before transferring to a TEM grid. The best efficiency of the full device structure was 2.4% after thermal annealing at 120–130 °C for 10 min. TEM imaging was carried out on a JEOL 2100F FEG TEM operating at 200 kV with Gatan Tridiem energy filter. Figure 1(a) shows an in-focus, unfiltered TEM image of the active layer prior to annealing, and Figure 1(b) is the corresponding energy filtered image acquired at the plasmon energy of 22 eV. The area imaged is virtually free of CZTS nanoparticles. A combination of low atomic number and similar composition makes it difficult to distinguish the P3HT and PCBM phases in the unfiltered image, but the contrast is significantly enhanced in the plasmon-loss image. In particular the structure consists of a dense network of semi-crystalline P3HT fibres.[9] The fibres are randomly oriented in projection, and there is no good evidence for bundling. The π-stacking

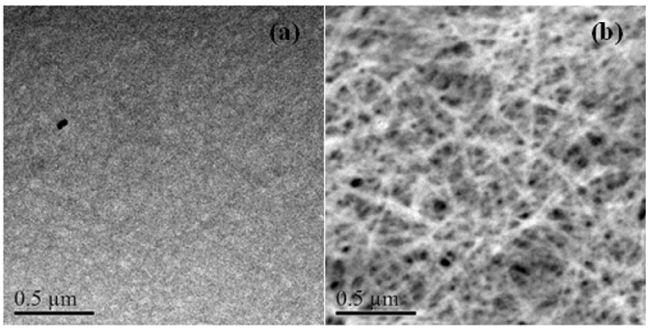

FIG. 1. (a) In-focus, unfiltered TEM image of the P3HT-PCBM thin-film and (b) the same area after plasmon-loss imaging (i.e., energy filtered by placing a 10 eV slit about the 22 eV plasmon peak).

within the P3HT fibres gives better hole mobility as well as stronger light absorption at red wavelengths. Furthermore the small diameter and high aspect ratio of the fibres mean that exciton dissociation is potentially more efficient, and a continuous percolation pathway is established for holes in suitably oriented fibres. All these factors combine to give better performing devices.[10] The grey background intensity between the fibres consists largely of PCBM (evidence for this will be presented later on). For an efficient device the space between the P3HT fibres must be filled with PCBM. Dark channels of very low intensity are also observed in Figure 1(b) (note, however, that the channel intensity in the 2D projected image is not zero). It is speculated that these channels are due to residual solvent trapped within a wet spin coated film[11] but have since evaporated by natural drying and/or electron beam irradiation in the TEM vacuum. In the study by Chang *et al.*,[11] however, the solvent was trapped within micrometer sized regions and was observable even under an optical microscope, whereas here the dimensions are on the nano-scale.

Electron energy loss spectroscopy (EELS) spectrum imaging in scanning TEM (STEM) mode was carried out to identify the individual phases. In spectrum imaging the focussed electron probe is rastered over the region of interest and an EELS spectrum acquired at each scan position. Figure 2(a) is a STEM bright field image of the P3HT-PCBM solar cell with the spectrum imaging region highlighted. As a first approximation a Gaussian peak was fitted to the plasmon feature at ~22 eV for each individual EELS spectrum in the spectrum image and from this the peak amplitude, full width at half maximum (FWHM) and peak centre extracted. These are shown in Figures 2(b)–2(d), respectively. As expected the peak amplitude is larger for the P3HT fibres, although there is an anti-correlation between peak amplitude and FWHM. EELS spectra were extracted from the regions marked "A" and "B" in Figure 2(b) and are shown superimposed in Figure 2(e). The spectra have been Fourier-log deconvolved to remove the zero loss peak[12] and are normalized with respect to the maximum intensity for visual comparison. The plasmon peak from region B is asymmetric and shows higher intensity at energies below the peak maximum. Comparison of peak shapes for pure P3HT and PCBM published in the literature[7,13] suggests that region B is PCBM-rich, the higher intensity of the plasmon peak at low energies being due to interband transitions in the constituent C_{60} molecule.[14] From Figure 2(c) the FWHM is largest within the channel regions, suggesting a higher PCBM concentration. PCBM has a higher solubility in chlorobenzene than P3HT,[15] so that the results are consistent with the hypothesis that the channels are due to residual solvent (the boiling point of chlorobenzene, 132 °C, is higher than toluene (110 °C) used for the CZTS nanoparticles). The regions between the channels and P3HT fibres show intermediate FWHM values, which suggest that they may contain PCBM as well as some amorphous P3HT intermixed at the molecular level.

In Figure 2(e) the two plasmon peak positions overlap at ~22 eV, while the reported peak position for P3HT is 22.2–23.4 eV and 25.5–26.0 eV for PCBM.[7,13] Several potential reasons can be put forward to explain the red shift in the PCBM plasmon peak. First the signal measured could be dominated by surface plasmons, especially if the PCBM is present as largely isolated molecules. For a sphere (e.g.,

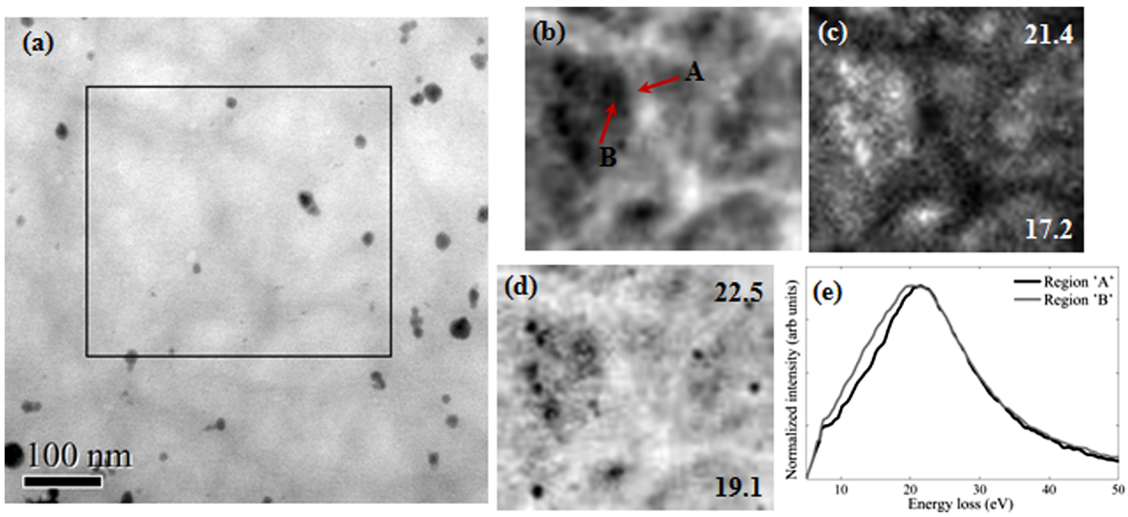

FIG. 2. (a) STEM bright field image of the P3HT-PCBM thin-film; the rectangular box shows the region for EELS spectrum imaging. The amplitude, FWHM, and centre of the Gaussian peak least squares fitted to the plasmon feature of each EELS spectrum in the spectrum image is shown in (b)–(d), respectively. The upper and lower numbers in (c)–(d) represent maximum and minimum values in eV for the FWHM and peak centre, respectively. Plasmon peaks extracted from regions "A" and "B" in Figure 2(b) are shown superimposed in (e). The zero loss peak has been removed via Fourier-log deconvolution, and the plasmon peak intensities have been normalized for direct comparison.

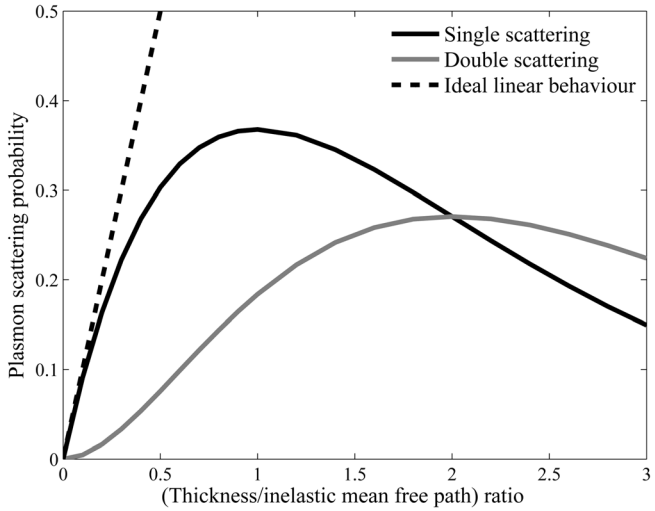

FIG. 3. Single and double plasmon scattering probability as a function of specimen thickness to inelastic mean free path ratio. The dashed line is a visual aid to demonstrate non-linear behaviour for single plasmon scattering.

C_{60} molecule) the surface dipole plasmon energy is reduced by a factor of $1/\sqrt{3}$ (=0.6) compared to the bulk plasmon energy; this red shift is too large to be consistent with the observations. Second if there is a high interfacial area between P3HT and PCBM then interfacial plasmons can contribute strongly. For a flat interface the interfacial loss function is proportional to $\mathrm{Im}\{-1/(\varepsilon_{\mathrm{P3HT}}+\varepsilon_{\mathrm{PCBM}})\}$, where ε is the dielectric function and "Im" represents the imaginary part.[12] The interfacial plasmon energy (as defined approximately by the zero crossing of the real part of ε with positive slope) should therefore be between pure P3HT and PCBM. This is not observed, and furthermore the signal from bulk PCBM at higher energies is also not present (Figure 2(e)). The third potential reason is the packing density of PCBM. A greater packing density results in a higher valence electron density and hence increased plasmon energy. The PCBM density is reported to vary between 1.3 and 1.5 g/cc,[16] so that by approximating PCBM to C_{60}, plasmon energies of 18.9–20.3 eV are calculated assuming a free electron model. The absolute value of the calculated plasmon energy is lower compared to experiment due to C_{60} interband transitions,[14] but nevertheless the range of permissible energies (1.4 eV) is of the order of the red shift observed in Figure 2(e). It is therefore suggested that the red shift is due to a lower PCBM packing density. This contributes to a lower plasmon intensity, so that contrast is generated between the P3HT fibres and surrounding PCBM in plasmon-loss images. The plasmon peak shape and position is proposed as a powerful tool to characterize PCBM and its packing density at the nanoscale in BHJ thin-films.

The high contrast of the plasmon-loss image enables a 3D electron tomography reconstruction of the P3HT-PCBM thin-film as first reported by Herzing *et al.*[7] However, the plasmon intensity follows a non-linear relationship with respect to specimen thickness (t) and is therefore not a valid signal for electron tomography. The probability for n plasmon scattering events P_n is given by Poisson statistics as $(1/n!)(t/\lambda)^n\exp(-t/\lambda)$.[12] Here λ is the plasmon mean free path and is approximately equal to the inelastic mean free path, i.e. the average distance the incident electron travels before losing energy to the solid. For the experimental conditions used in this study $\lambda \sim 110$ nm for carbon-rich materials.[12] Figure 3 shows the probability for single and double plasmon scattering as a function of (t/λ). For $(t/\lambda) \rightarrow 1$ the single scattering intensity deviates from ideal linear behaviour, while for, $(t/\lambda) > 1$ monotonic behaviour is no longer observed due to multiple scattering. Organic BHJ solar cells are made deliberately "thick" ($\sim$100 nm) in order to efficiently absorb the incident light, so that even at zero tilt $(t/\lambda) \approx 1$. Thickness corrections are therefore essential for tomographic reconstructions to be meaningful. It can be shown that $(t/\lambda) = \ln(I_t/I_o)$, where I_t is the total transmitted electron intensity and I_o is the "zero loss" intensity of electrons that have lost no energy.[12] At each specimen tilt in a tomography experiment two further images are therefore acquired in addition to the plasmon-loss image: an unfiltered image for I_t and an "elastic" image for I_o by placing a 10 eV slit over the zero loss peak in the EELS spectrum. (t/λ) can then be calculated for each image pixel using the unfiltered and elastic images; this enables the 22 eV plasmon-loss image to be corrected for thickness using the Poisson distribution for single scattering (i.e., $(t/\lambda)\exp(-t/\lambda)$; note that the double scattering intensity is present at twice the energy value of the (22 eV) single scattering plasmon and so on). In a composite material such as P3HT and PCBM the (t/λ) thickness correction is, strictly speaking, only approximate, since λ will vary between the two phases. However, this variation in λ is small as both phases are carbon-rich, with the other constituent elements being of similar low atomic number. Since thickness is approximately corrected at the *local* level other potential effects, such as surface roughening due to P3HT crystallisation,[17] are also accounted for.

Electron tomography was carried out by tilting the specimen between $-56°$ and $52°$ at $2°$ tilt intervals. A 10 eV slit centred about 22 eV was used to form the plasmon-loss image. (t/λ) for the specimen at zero tilt was only $\sim$0.1, indicating that the specimen was considerably thinner than the

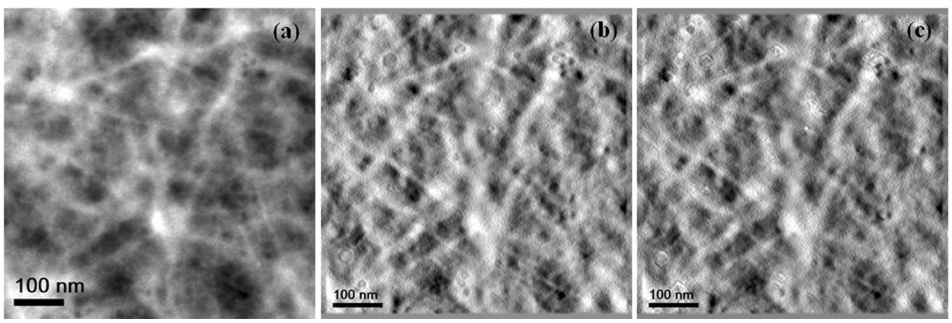

FIG. 4. (a) Zero tilt image of the region used for the tomographic reconstruction. (b) and (c) show equivalent ortho-slices extracted from the 3D reconstructed (20 SIRT iterations) tomograms with and without the (t/λ) thickness correction, respectively (enhanced online) [URL: http://dx.doi.org/10.1063/1.4812485.1].

ideal active layer. Some sputtering of the BHJ thin-film took place upon prolonged beam exposure, but the tomography acquisition dose was kept sufficiently low so as to minimize its effects. The tilt series images were accurately aligned using CZTS nanoparticle positions in the corresponding unfiltered images via the Penczek algorithm[18] (gold particles can be used for BHJ solar cells lacking internal markers). Figure 4(a) shows the region used for tomographic reconstruction and was extracted from the plasmon-loss image at zero tilt. Figures 4(b) and 4(c) are equivalent ortho-slices extracted from the tomographic reconstructions before and after the (t/λ) thickness correction, respectively. The two reconstructions are very similar due to the small thickness of the BHJ film, although a slight improvement in contrast was observed in the high tilt images after thickness correction. A comparison with the plasmon-loss image at zero tilt (Figure 4(a)) shows that the nano-scale features are largely reproduced. In practice however P3HT fibres lying perpendicular to the tilt axis will only be weakly reconstructed due to their shape transform overlapping with the tomography "missing wedge" (i.e., the angular range over which projection images are not acquired). P3HT fibres of diameter ~6 nm and above are resolved in the tomograms. For the experimental conditions used in this study (i.e., no objective aperture) the theoretical spatial resolution[19] for the plasmon-loss image is estimated to be ~5 nm, with the dominant contribution being chromatic aberration of the objective lens. The best attainable resolution is ~2 nm for a 10 mrad objective aperture; in this new regime plasmon delocalisation is the limiting factor. In practice the use of a smaller objective aperture would limit the collection efficiency, so that any resolution enhancement may be masked by reduced signal-to-noise ratio. Furthermore the final tomogram resolution will also be less than that of the projected images, due to errors in image alignment as well as missing wedge artefacts. If electron dose was not an issue the tomogram resolution can be improved by acquiring a larger tilt series by increasing the tilt angle range and/or decreasing the tilt angle step size. Radiolysis and sputtering both occur in the BHJ thin-film; the former leads to a rapid loss of crystalline reflections from the P3HT fibres in the diffraction pattern but has no discernible effect on the plasmon-loss image. Sputtering is however a problem and can be reduced by lowering the electron beam accelerating voltage. This effectively increases the inelastic mean free path for a given specimen thickness, so that (t/λ) thickness corrections become increasingly important.

In summary the EELS plasmon signal has revealed a wealth of information about P3HT-PCBM solar cells, including phase identification, PCBM packing density and presence of open channels due to residual solvent. It is a powerful tool for investigating the effects of thermal, solvent annealing and solvent additives on BHJ morphology at the nano-scale. A robust plasmon-loss tomography technique has also been developed that takes into account non-linear thickness effects. The technique has been shown to reproduce the nano-scale morphological features, subject to the constraints of the missing wedge and intrinsic factors limiting spatial resolution.

[1]B. C. Thompson and J. M. J. Fréchet, Agnew. Chem., Int. Ed. **47**, 58 (2008).
[2]T. Wang, A. J. Pearson, D. G. Lidzey, and R. A. L. Jones, Adv. Funct. Mater. **21**, 1383 (2011).
[3]G. Li, Y. Yao, H. Yang, V. Shrotriya, G. Yang, and Y. Yang, Adv. Funct. Mater. **17**, 1636 (2007).
[4]J. K. Lee, W. L. Ma, C. J. Brabec, J. Yuen, J. S. Moon, J. Y. Kim, K. Lee, G. C. Bazan, and A. J. Heeger, J. Am. Chem. Soc. **130**, 3619 (2008).
[5]S. S. van Bavel and J. Loos, Adv. Funct. Mater. **20**, 3217 (2010).
[6]S. S. van Bavel, E. Sourty, G. de With, and J. Loos, Nano Lett. **9**, 507 (2009).
[7]A. A. Herzing, L. J. Richter, and I. M. Anderson, J. Phys. Chem. C **114**, 17501 (2010).
[8]Q. Guo, H. W. Hillhouse, and R. Agrawal, J. Am. Chem. Soc. **131**, 11672 (2009).
[9]M. Brinkman and J. C. Wittmann, Adv. Mater. **18**, 860 (2006).
[10]S. Berson, R. De Bettignies, S. Bailly, and S. Guillerez, Adv. Funct. Mater. **17**, 1377 (2007).
[11]L. Chang, H. W. A. Lademann, J. B. Bonekamp, K. Meerholz, and A. J. Moulé, Adv. Funct. Mater. **21**, 1779 (2011).
[12]R. F. Egerton, *Electron Energy-Loss Spectroscopy in the Electron Microscope*, 2nd ed. (Plenum Press, New York, 1996).
[13]J. A. Amonoo, E. Glynos, X. C. Chen, and P. F. Green, J. Phys. Chem. C **116**, 20708 (2012).
[14]R. Kuzuo, M. Terauchi, M. Tanaka, Y. Saito, and H. Shinohara, Jpn. J. Appl. Phys. **30**, L1817 (1991).
[15]L. Li, H. Tang, H. Wu, G. Lu, and X. Yang, Org. Electron. **10**, 1334 (2009).
[16]J. W. Kiel, B. J. Kirby, C. F. Majkrzak, B. B. Maranville, and M. E. Mackay, Soft Matter **6**, 641 (2010).
[17]G. Li, V. Shrotriya, Y. Yao, J. Huang, and Y. Yang, J. Mater. Chem. **17**, 3126 (2007).
[18]P. Penczek, M. Marko, K. Buttle, and J. Frank, Ultramicroscopy **60**, 393 (1995).
[19]O. L. Krivanek, M. K. Kundmann, and K. Kimoto, J. Microsc. **180**, 277 (1995).